

# *Uncertainty in the evolution of climate feedback traced to the strength of the Atlantic Meridional Overturning Circulation*

Article

Accepted Version

Lin, Y.-J., Hwang, Y.-T., Ceppi, P. and Gregory, J. ORCID: <https://orcid.org/0000-0003-1296-8644> (2019) Uncertainty in the evolution of climate feedback traced to the strength of the Atlantic Meridional Overturning Circulation. *Geophysical Research Letters*, 46 (21). pp. 12331-12339. ISSN 1944-8007 doi: <https://doi.org/10.1029/2019GL083084> Available at <https://centaur.reading.ac.uk/86746/>

It is advisable to refer to the publisher's version if you intend to cite from the work. See [Guidance on citing](#).

To link to this article DOI: <http://dx.doi.org/10.1029/2019GL083084>

Publisher: AGU

All outputs in CentAUR are protected by Intellectual Property Rights law, including copyright law. Copyright and IPR is retained by the creators or other copyright holders. Terms and conditions for use of this material are defined in the [End User Agreement](#).

[www.reading.ac.uk/centaur](http://www.reading.ac.uk/centaur)

**CentAUR**

Central Archive at the University of Reading

Reading's research outputs online

1 **Uncertainty in the evolution of climate feedback traced to the strength of the Atlantic**  
2 **Meridional Overturning Circulation**

3 **Yuan-Jen Lin<sup>1</sup>, Yen-Ting Hwang<sup>1†</sup>, Paulo Ceppi<sup>2</sup>, and Jonathan Gregory<sup>3,4</sup>**

4 <sup>1</sup>Department of Atmospheric Sciences, National Taiwan University, Taiwan

5 <sup>2</sup>Grantham Institute, Imperial College London, United Kingdom

6 <sup>3</sup>NCAS-Climate, University of Reading, Reading, United Kingdom

7 <sup>4</sup>Met Office Hadley Centre, Exeter, United Kingdom

8  
9 †Corresponding author: Yen-Ting Hwang ([ythwang@ntu.edu.tw](mailto:ythwang@ntu.edu.tw))

10 **Key Points:**

- 11 • Uncertainty in the Atlantic Meridional Overturning Circulation is the main cause of the  
12 model spread in evolution of the warming pattern.
- 13 • Warming in Northern Hemisphere extratropics tends to be surface trapped, leading to  
14 more positive lapse-rate and cloud feedbacks.
- 15 • Models with stronger recovery in Atlantic Meridional Overturning Circulation tend to  
16 project a larger increase in net climate feedback.

## 17 **Abstract**

18 In most coupled climate models, effective climate sensitivity increases for a few decades  
19 following an abrupt CO<sub>2</sub> increase. The change in the climate feedback parameter between the first  
20 20 years and the subsequent 130 years is highly model-dependent. In this study, we suggest that  
21 the intermodel spread of changes in climate feedback can be partially traced to the evolution of the  
22 Atlantic Meridional Overturning Circulation (AMOC). Models with stronger AMOC recovery  
23 tend to project more amplified warming in the Northern Hemisphere a few decades after a  
24 quadrupling of CO<sub>2</sub>. Tropospheric stability then decreases as the Northern Hemisphere gets  
25 warmer, which leads to an increase in both the lapse-rate and shortwave cloud feedbacks. Our  
26 results suggest that constraining future ocean circulation changes will be necessary for accurate  
27 climate sensitivity projections.

## 28 **Plain Language Summary**

29 How much the Earth's climate will warm in response to increasing carbon dioxide  
30 concentration, a number known as climate sensitivity, is an essential metric of the impacts of  
31 anthropogenic climate change. Most current global climate models agree that the climate will  
32 become more sensitive as time passes, indicating an underestimation of future warming inferred  
33 from historical records. In this study, we report that the slow response of oceanic circulation has  
34 an influence on this time evolution of climate sensitivity. In the 15 state-of-the-art global climate  
35 models we investigate, the models projecting re-strengthening of Atlantic Meridional Overturning  
36 Circulation (AMOC) after a few decades of weakening tend to simulate a more significant increase  
37 in climate sensitivity. We propose a mechanism as follows: AMOC strengthening causes more  
38 enhanced surface warming in the Northern Hemisphere, altering the vertical stability of the global  
39 atmosphere. The changes in atmospheric vertical stability then strengthen the radiative feedbacks  
40 that amplify greenhouse gas forcing, accounting for the larger increase in climate sensitivity in  
41 these models. Our findings emphasize the important contribution of ocean circulation to the  
42 intermodel spread in climate change projections.

## 43 **1 Introduction**

44 Equilibrium climate sensitivity (ECS) refers to the globally-averaged equilibrium surface  
45 air temperature response to an abrupt doubling of CO<sub>2</sub> concentration, and it has spanned a range  
46 of 1.5 – 4.5 K for decades (Charney et al., 1979; Flato et al., 2013). Since it takes thousands of  
47 years for coupled models to reach steady state, ECS is usually estimated by assuming the net  
48 climate feedback ( $\lambda$ ) is time-invariant (Gregory et al., 2004):

$$49 \text{ECS} = -F/\lambda. \quad (1)$$

50 F is radiative forcing of 2×CO<sub>2</sub>. The “constant  $\lambda$ ” approximation has been applied to some  
51 atmospheric general circulation models (AGCMs) coupled to slab ocean models, pointing out that  
52 the uncertainty in cloud feedback is the main cause of the intermodel spread of ECS (Bony et al.,  
53 2006). Many studies, however, have reported a time dependence of  $\lambda$  in atmosphere–ocean  
54 coupled general circulation models (AOGCMs), which adds another uncertainty in determining  
55 ECS (Block & Mauritsen, 2013; Geoffroy et al., 2013; Armour, 2017). The time dependence of  $\lambda$   
56 has been related to the evolution of the surface warming pattern (Armour et al., 2013; Rose et al.,  
2014; Zhou et al., 2016).

58 How the surface warming pattern evolves under CO<sub>2</sub> forcing and how it varies among  
59 models are further issues to be confronted in narrowing the uncertainty of ECS. Many have argued  
60 for the importance of the ocean in controlling the surface warming pattern (Winton et al., 2010;

61 Winton et al., 2013; Marshall et al., 2015). For example, Marshall et al. (2015) observed a broad  
 62 correspondence in SST anomaly between the ocean-only model and multiple AOGCMs, especially  
 63 the delayed warming in the North Atlantic and the Southern Ocean, suggesting that mechanisms  
 64 controlling the SST response in coupled models are influenced by ocean processes.

65 To identify the mechanisms driving the distinct time evolution of climate feedbacks across  
 66 AOGCMs, we diagnose the time-varying ocean processes, surface warming patterns, and climate  
 67 feedbacks in fully coupled models (section 2). We show that part of the intermodel spread in  
 68 climate feedback evolution can be traced to the evolution of the Atlantic Meridional Overturning  
 69 Circulation (AMOC), via changes in the surface warming pattern and atmospheric stability  
 70 (section 3). In section 4 we summarize our results and compare them with the previous studies  
 71 focusing on the multimodel mean.

## 72 **2 Materials and Methods**

### 73 **2.1 Model data**

74 We analyze the output from 15 climate models participating in the Coupled Model  
 75 Intercomparison Project Phase 5 (CMIP5) that provide the required variables for our study (Table  
 76 S1). 150-year simulations with pre-industrial conditions (piControl) and forced with an abrupt  
 77 quadrupling of atmospheric CO<sub>2</sub> concentration (abrupt4×CO<sub>2</sub>) are assessed. To remove any model  
 78 drift, we calculate the anomalies by subtracting the piControl integration from the corresponding  
 79 parallel abrupt4×CO<sub>2</sub> integration.

### 80 **2.2 The evolution of the climate system per 1K global warming**

81 To represent the evolution of the climate system, we define an operator "δ" as follows:

$$82 \quad \delta X = \left. \frac{dX}{d(\text{GMT})} \right|_{Y21-150} - \left. \frac{dX}{d(\text{GMT})} \right|_{Y1-20}. \quad (2)$$

83 X can be any of the target fields. Ordinary least-squares regression of annual-mean anomalies in  
 84 X against annual- and global-mean surface air temperature anomaly (GMT) is separately done for  
 85 the early (years 1-20) and late (years 21-150) periods. The separation at year 20 approximately  
 86 divides climate responses into fast and slow components (Held et al., 2010; Geoffroy et al., 2013).  
 87 When X is surface air temperature (TAS), equation (2) gives the "surface warming pattern  
 88 evolution" (δTAS) (Figure 2a). When X is the global-mean net radiation at the TOA, the terms in  
 89 equation (2) are the net climate feedback (λ) for the two time periods, and the difference gives the  
 90 "net climate feedback evolution" (δλ). Different choices of separation year have little influence  
 91 on the magnitudes of δλ (Andrews et al., 2015). δλ can be further decomposed into various  
 92 components using the radiative kernel method (Soden et al. (2008); see Text S1).

93 The terms in equation (2) are chosen to be derivatives with respect to GMT for two reasons  
 94 (see Figure S1 for GMT evolution). First, the patterns of surface temperature and TOA radiation,  
 95 expressed per unit of GMT increase, are generally assumed to be constant in a given model. This  
 96 is an application of the common "pattern scaling" assumption. If pattern scaling holds exactly for  
 97 X, equation (2) gives δX=0; otherwise, δX measures the deviation from pattern scaling. Second,  
 98 the change in any X tends to be larger for models which have greater ECS, and hence greater GMT  
 99 at all time. The use of the derivatives thus in effect normalizes δX with respect to ECS, removing  
 100 that factor from the consideration of the spread among models in the projected changes.

101 2.3 AMOC index ( $\delta\psi$ )

102 For each model, we first identify the AMOC strength ( $\psi$ ) as the maximum of the ocean  
103 overturning mass streamfunction (variable name *msftmyz* or *msftyyz*) over the North Atlantic (north  
104 of 30°N), excluding the overturning shallower than 500 m (Gregory et al., 2005). We then define  
105 the “AMOC index ( $\delta\psi$ )” as per equation (2) with X as the AMOC strength ( $\psi$ ). The AMOC index  
106 quantifies the AMOC evolution from early to late periods in each model and is insensitive to the  
107 choice of separation year discussed in section 2.2 (Table S2). Variations in AMOC strength arising  
108 from natural variability tend to be substantially smaller than AMOC index values and are unlikely  
109 to explain the intermodel spread (see Text S2). With regard to our motivation for taking derivatives  
110 with respect to GMT (cf. the previous paragraph), there is no significant correlation of AMOC  
111 changes with ECS across models, so the second reason does not apply. The first reason is valid  
112 because it makes the early and late terms comparable, by normalizing responses with respect to  
113 the magnitude of climate change in the two periods.

114 **3 Results**

115 On average in the 15 CMIP5 coupled climate models analyzed in this study, the climate  
116 system becomes more sensitive as it approaches equilibrium, with the multimodel-mean net  
117 climate feedback ( $\lambda$ ) evolving from  $-1.37 \text{ Wm}^{-2}\text{K}^{-1}$  during the first 20 years of abrupt4×CO<sub>2</sub>  
118 simulations to  $-0.87 \text{ Wm}^{-2}\text{K}^{-1}$  during the following 130 years. The difference in multimodel-  
119 mean  $\lambda$  ( $0.50 \text{ Wm}^{-2}\text{K}^{-1}$ ) between the periods is consistent with previous studies (Andrews et al.,  
120 2015; Ceppi & Gregory, 2017). At the same time, this time evolution of climate feedback ( $\delta\lambda$ ) is  
121 highly model-dependent, ranging from  $-0.18$  to  $1.05 \text{ Wm}^{-2}\text{K}^{-1}$  across models, a range 2.5 times  
122 as large as the magnitude of their multimodel mean.

123 To identify the root cause of the intermodel spread of climate feedback evolution, we  
124 investigate the evolution of global meridional overturning circulation (GMOC), quantified as the  
125 meridional mass streamfunction for the global ocean (Manabe & Stouffer, 1993; Talley et al.,  
126 2003). An Empirical Orthogonal Function (EOF) analysis (also known as Principal Component  
127 Analysis) of GMOC evolution, applied across models, shows that the AMOC evolution is the main  
128 uncertainty of the global ocean circulation response (see Text S3). This is consistent with previous  
129 studies highlighting the uncertainty in AMOC projections in CMIP5 models (Cheng et al., 2013;  
130 Wang et al., 2014; Heuzé et al., 2015). Based on the AMOC evolution, the 15 CMIP5 models can  
131 be classified into three groups, with high, medium, and low AMOC indices ( $\delta\psi$ ; see Figure S2 for  
132 the list of models in each composite). In the high AMOC index composite, the AMOC slows down  
133 significantly in the initial stage of warming but recovers in strength in the later stage; by contrast,  
134 in the low AMOC index composite, the AMOC slows down moderately in the initial warming but  
135 continues slowing down as warming proceeds (Figure 1a). It is possible that models in the low  
136 index group would eventually project AMOC re-strengthening if the lengths of the simulations  
137 were extended. The timing of the re-strengthening could be more than a thousand years after  
138 quadrupling CO<sub>2</sub> (Stouffer & Manabe, 2003; Li et al., 2013). The weakening of the AMOC in  
139 response to greenhouse-gas forcing is predominantly due to the buoyancy effect of changes in  
140 surface heat flux, with the effect of changes in surface water flux being relatively minor (Gregory  
141 et al., 2005; Gregory et al., 2016). However, substantially increased meltwater from the Greenland  
142 ice sheet, not included in CMIP5 experiments, could further weaken the AMOC (Stouffer et al.,  
143 2006; Swingedouw et al., 2009; Sgubin et al., 2015; Swingedouw et al., 2015; Saenko et al., 2017).

144 The cause of the intermodel spread in AMOC evolution is beyond the scope of this study.  
145 Instead, we report that the spread in the AMOC evolution can partly contribute to the intermodel  
146 spread in net climate feedback evolution ( $\delta\lambda$ ).  $\delta\lambda$  is positively correlated with the AMOC index  
147 ( $\delta\psi$ ) ( $r=0.55$ ; Figure 1b). In the rest of the paper, we will explain why models with higher AMOC  
148 index tend to project a larger increase in  $\lambda$  through changes in surface warming pattern and  
149 tropospheric stability.

### 150 3.1 The uncertainty in the surface warming pattern evolution ( $\delta$ TAS)

151 As the climate system approaches equilibrium, the multimodel-mean surface warming  
152 pattern becomes less pronounced over the Arctic region and the western North Pacific, and more  
153 pronounced over the tropical East Pacific and the Southern Ocean (Figure 2a), consistent with  
154 Andrews et al. (2015) and Ceppi and Gregory (2017). In most regions over the globe, we note that  
155 the evolution of the surface warming pattern ( $\delta$ TAS) is quite model-dependent, since the  
156 magnitudes of 1 standard deviation of  $\delta$ TAS across models are larger than the multimodel-mean  
157  $\delta$ TAS. In addition, the first EOF of  $\delta$ TAS across models, explaining 48% of the total variance,  
158 exhibits a difference between the northern and southern hemispheres (Figure 2b), suggesting that  
159 the degree of hemispheric asymmetry is the main uncertainty in the evolution of the surface  
160 warming pattern.

161 We propose that the intermodel spread of the AMOC evolution is a cause of the spread in  
162  $\delta$ TAS. To visualize the spatial pattern of the AMOC-related  $\delta$ TAS spread, Figure 2c shows the  
163 regression slopes of  $\delta$ TAS against the AMOC index. Models with higher AMOC index tend to  
164 project increasingly pronounced warming in the Northern Hemisphere (NH) extratropics, and  
165 increasingly weak warming in the tropics and Southern Hemisphere (SH) as time passes, and vice  
166 versa for models with lower AMOC index (Figures 2c and 2d). Note the remarkable similarity  
167 between the AMOC-related spread of  $\delta$ TAS (Figure 2c) and the first EOF of  $\delta$ TAS (Figure 2b)  
168 (area-weighted pattern correlation = 0.94). Also, the AMOC index is well correlated with the  
169 principal component (PC) corresponding to the first EOF (Figure 2e). We therefore suggest that  
170 the varying AMOC evolution is the main cause for the uncertainties in the warming pattern  
171 evolution ( $\delta$ TAS). Previous studies have attributed the surface temperature response on decadal  
172 and longer timescales to the strength of the deep ocean circulation, based on results from a single  
173 model or from the CMIP5 multimodel-mean (Marshall et al., 2015; Trossman et al., 2016). Here  
174 we corroborate that attribution by relating the intermodel spread of the surface warming pattern  
175 evolution to the varying AMOC evolution among models.

### 176 3.2 The uncertainty in the tropospheric stability evolution ( $\delta$ EIS)

177 Varying hemispheric asymmetry in the surface warming pattern evolution can lead to  
178 uncertainty in the tropospheric stability response, shown to be a key mechanism for the time  
179 evolution of climate feedbacks (Ceppi & Gregory, 2017; Andrews & Webb, 2018). Here we  
180 quantify tropospheric stability by calculating the estimated inversion strength (EIS), defined as the  
181 difference in potential temperature between 700 hPa and the surface, corrected to account for the  
182 dependence of the moist adiabat on mean temperature (Wood & Bretherton, 2006). In general, the  
183 multimodel-mean EIS evolution ( $\delta$ EIS, defined using equation (2)) has the opposite sign from the  
184 multimodel-mean warming pattern evolution ( $\delta$ TAS) (Figure S3, consistent with Figure 1b in  
185 Ceppi and Gregory (2017)). Also, similar to  $\delta$ TAS,  $\delta$ EIS appears to be model-dependent. For  
186 example, in the Arctic, the North Atlantic, and the western North Pacific, the negative regression  
187 slopes indicate that models with stronger AMOC recovery (high AMOC index) tend to project an

188 increasingly unstable troposphere in these regions, and vice versa for the positive regression slopes  
189 in the tropical South Atlantic (Figure 3a). Dominated by the negative correlation in the NH, Figure  
190 3c shows that the global-mean EIS evolution negatively correlates with the AMOC index.

191 Our interpretation for the link between hemispherically asymmetric warming pattern and  
192 global EIS response is as follows. The pronounced warming in the relatively stable NH extratropics  
193 tends to remain trapped near the surface, resulting in a more unstable troposphere. The warming  
194 is increasingly pronounced if the AMOC index is higher, accounting for the negative regression  
195 slopes of  $\delta\text{EIS}$  against the AMOC index. In the tropics, consistent with the weak temperature  
196 gradient approximation (Sobel et al., 2002), the temperature of the free troposphere is uniform and  
197 is determined by the SST over the deep convective regions (e.g., the West Pacific warm pool),  
198 where the lapse rate is close to a moist adiabat. The regression slopes of  $\delta\text{TAS}$  against the AMOC  
199 index are negative in the West Pacific warm pool (Figure 2c). The approximation explains a larger  
200 decrease in temperature of the free troposphere throughout the entire tropics for models with higher  
201 AMOC index (not shown). Therefore, regions with positive or insignificant regression slopes of  
202  $\delta\text{TAS}$  against AMOC index exhibit negative regression slopes of  $\delta\text{EIS}$ . Consistently, Figure 3a  
203 shows that regions with more positive  $\delta\text{TAS}$  relative to the warm pool (red contours) would project  
204 more negative  $\delta\text{EIS}$ , and vice versa for the regions with more negative  $\delta\text{TAS}$  relative to the warm  
205 pool (green contours). An exception to this behavior is in the SH extratropics, where the suppressed  
206 warming response over Antarctica is not trapped near the surface as in the NH extratropics. Instead,  
207 it is vertically uniform and can be ascribed to a more positive southern hemisphere annular mode  
208 (SAM). A more positive SAM is characterized by the band of westerly winds contracting toward  
209 Antarctica (Figure 3e) and is associated with equivalent barotropic wind and temperature  
210 anomalies (Thompson & Wallace, 2000).

### 211 3.3 The uncertainty in the climate feedback evolution ( $\delta\lambda$ )

212 The AMOC-related spread in global EIS evolution affects the lapse-rate feedback. Figure  
213 4a shows the regression slopes of lapse-rate feedback evolution against the AMOC index, which  
214 is strongly anticorrelated with the regression slopes of the EIS evolution (Figure 3a) (area-  
215 weighted pattern correlation = -0.92). In the Arctic, the North Atlantic, and most of the North  
216 Pacific, the troposphere becomes more unstable in the models with higher AMOC index. A more  
217 unstable troposphere indicates a reduced cooling ability of the free troposphere, which then results  
218 in a more positive lapse-rate feedback. Since models with a more positive AMOC index tend to  
219 project a larger decrease in global-mean EIS (Figure 3c), those models should also feature a larger  
220 increase in global-mean lapse-rate feedback. Indeed, Figure 4c shows a positive correlation ( $r=0.83$ )  
221 between the AMOC index and the global-mean change in lapse-rate feedback. In summary, models  
222 with a higher AMOC index tend to project a stronger decrease in the NH tropospheric stability  
223 while having little influence on the vertical temperature profile in the SH. This hemispherically  
224 asymmetric amplitude of stability response to the varying AMOC evolution results in global-mean  
225 changes in EIS and lapse-rate feedback against the AMOC index.

226 Meanwhile, the EIS evolution also contributes to the evolution of shortwave cloud  
227 feedback in specific regions. Figure 4d shows that shortwave cloud feedback becomes more  
228 positive in the North Atlantic and the North Pacific mid-latitudes, where  $\delta\text{EIS}$  is negative. The  
229 destabilization of the lower troposphere acts to reduce low cloud cover, which leads to a more  
230 positive shortwave cloud feedback, associated with a higher AMOC index. In the tropics, the  
231 degree of ITCZ shift affects the shortwave cloud feedback. Consistent with the energetic  
232 framework (Kang et al., 2008; Kang et al., 2009; Friedman et al., 2013), models with higher



233 AMOC index, tending to project NH warming, produce a weaker southward ITCZ shift (Figure  
234 S4), which results in a more negative (positive) shortwave cloud feedback in the north (south)  
235 (Figures 4d and 4e). With positive and negative values generally cancelling out, the AMOC-related  
236 spread in tropical mean shortwave cloud feedback evolution contributes little to the global-mean  
237 change. Instead, it is the spread in the NH mid-latitudes that largely makes up the positive  
238 correlation between the AMOC index and the global-mean change in shortwave cloud feedback  
239 (Figure 4f). While some of the spread in shortwave cloud feedback is compensated by the spread  
240 in longwave cloud feedback, we note that this compensation mostly happens in the tropics (Figure  
241 S5g). In the extratropics, the change in net cloud feedback is dominated by the shortwave  
242 component (Figure S5j). Thus, the mechanism described above may explain the positive  
243 correlation between the AMOC index and the area-averaged net cloud feedback evolution  
244 poleward of 30 degrees ( $r=0.61$ ). Apart from the influence of tropospheric stability mentioned here,  
245 we note that the intermodel spread of cloud feedback could arise from a dependence on  
246 parameterization and resolution (Vial et al., 2013; Webb et al., 2015).

247 In addition to lapse-rate and cloud feedbacks, the AMOC evolution also has an impact on  
248 other feedback components. In models with stronger AMOC recovery, for example, albedo  
249 feedback becomes more positive in the NH polar region due to more melting ice, where the  
250 enhanced warming occurs, and vice versa for the SH polar region with smaller magnitudes (Figure  
251 S5a). Similar to longwave cloud feedback, the relative humidity feedback evolves toward more  
252 positive (negative) values in the NH (SH) tropics, indicating a northward shift of the ITCZ (Figure  
253 S5d). While the varying AMOC evolution influences the pattern evolution of these two feedbacks,  
254 the correlations between the AMOC index and the global-mean changes in relative humidity and  
255 surface albedo feedbacks are not significant (Figures S5c and S5f). Also, we note that the  
256 relationship between the AMOC index and the changes in most of the climate feedback  
257 components cannot be explained if assuming time-invariant local feedbacks (Armour et al., 2013).  
258 Instead, the evolution of tropospheric stability introduces nonlinearity in local climate feedbacks  
259 (Zhou et al., 2016; Ceppi & Gregory, 2017) (see Text S4).

#### 260 **4 Summary and discussion**

261 In this study, we suggest that the intermodel spread in net climate feedback evolution ( $\delta\lambda$ )  
262 can be partially traced to the evolution of the AMOC strength. Models with stronger AMOC  
263 recovery tend to project a larger increase in net climate feedback, indicating more sensitive climate  
264 over longer timescales. The interpretation for the link between the AMOC evolution and the  
265 feedback change is as follows: the strengthening of AMOC over long timescales shifts the location  
266 of warming to NH extratropical regions, leading to a global destabilization of the troposphere, and  
267 resulting in more positive lapse rate and shortwave cloud feedbacks. Similar relationships between  
268 AMOC strength and radiative anomalies are also found in decadal-scale unforced variability in the  
269 piControl simulations (see Text S5).

270 Interestingly, our interpretation that warmer NH leads to more sensitive climate cannot be  
271 applied to understanding the evolution of the multimodel-mean climate feedback. For the  
272 multimodel-mean, the increase in  $\lambda$  is accompanied by enhanced warming mostly in the SH,  
273 especially in the tropical Southeast Pacific and the Southern Ocean (Figure 2a). In our analysis of  
274 the intermodel spread, the warming pattern evolution among models includes varying degrees of  
275 the north-south contrast (Figure 2b), which contributes to the intermodel spread of the global EIS  
276 response and the climate feedback evolution.

277 The dependence of climate feedbacks on the surface warming pattern has been an active  
 278 research area. Some studies have focused on the east-west contrast of the surface warming pattern  
 279 (Ceppi & Gregory, 2017; Zhou et al., 2017; Andrews & Webb, 2018); for example, Zhou et al.  
 280 (2017) suggest that the cloud feedback is more negative in response to western Pacific warming,  
 281 and more positive in response to warming in the eastern Pacific. On the other hand, others  
 282 emphasize the tropics-extratropics contrast, suggesting that the climate will become more sensitive  
 283 as the ocean heat uptake pattern evolves (Rose et al., 2014; Rugenstein et al., 2016; Liu et al.,  
 284 2018a; Liu et al., 2018b). By investigating the cause of inter-model spread in the time dependence  
 285 of climate feedbacks, we identify an additional geographical structure for controlling global-mean  
 286 climate feedbacks: the variation of SST in the more stable NH high latitudes tends to be more  
 287 confined in the lower troposphere than the variation of SST in the SH counterparts and is more  
 288 likely to trigger positive radiative feedbacks. In future work, idealized experiments will be needed  
 289 to provide a full understanding of the influence of SST patterns on climate feedbacks.

## 290 **Acknowledgments**

291 We thank three anonymous reviewers for constructive comments, and Angie Pendergrass  
 292 for providing radiative kernels. We acknowledge the World Climate Research Programme's  
 293 Working Group on Coupled Modelling, which is responsible for CMIP, and we thank the climate  
 294 modeling groups (listed in Table S1) for producing and making available their model output. For  
 295 CMIP, the U.S. DOE's Program for Climate Model Diagnosis and Intercomparison provided  
 296 coordinating support and led development of software infrastructure in partnership with the Global  
 297 Organization for Earth System Science Portals. Additional derived data and materials are available  
 298 from YTH.

299 YJL and YTH were supported by Ministry of Science and Technology of Taiwan (MOST  
 300 107-2636-M-002-001 and MOST 108-2636-M-002-007). PC is supported by an Imperial College  
 301 Research Fellowship. JMG was supported by the European Research Council under the European  
 302 Union's Horizon 2020 research and innovation programme (grant agreement no. 786427, project  
 303 "Couplet").

## 304 **References**

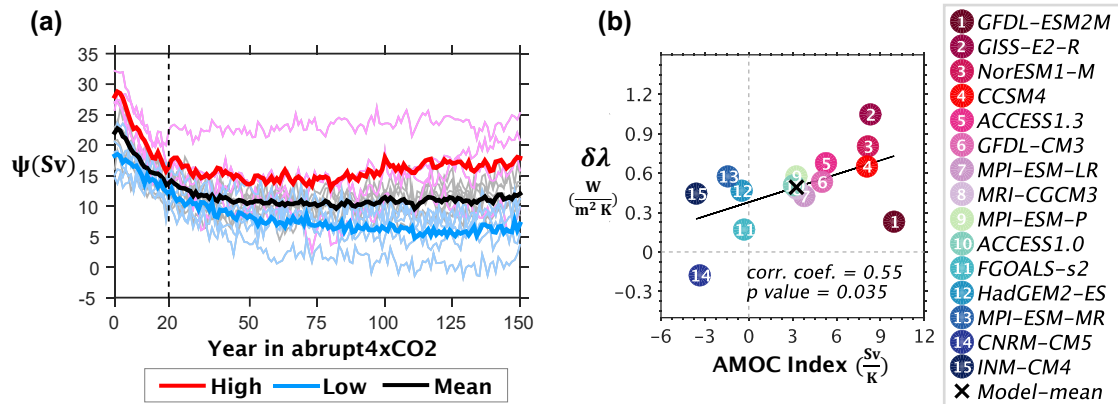
- 305 Andrews, T., Gregory, J. M., & Webb, M. J. (2015). The Dependence of Radiative Forcing and Feedback on  
 306 Evolving Patterns of Surface Temperature Change in Climate Models. *Journal of Climate*, 28(4), 1630-  
 307 1648. doi:10.1175/Jcli-D-14-00545.1
- 308 Andrews, T., & Webb, M. J. (2018). The Dependence of Global Cloud and Lapse Rate Feedbacks on the Spatial  
 309 Structure of Tropical Pacific Warming. *Journal of Climate*, 31(2), 641-654.
- 310 Armour, K. C. (2017). Energy budget constraints on climate sensitivity in light of inconstant climate feedbacks.  
 311 *Nature Climate Change*, 7(5), 331-335.
- 312 Armour, K. C., Bitz, C. M., & Roe, G. H. (2013). Time-varying climate sensitivity from regional feedbacks. *Journal*  
 313 *of Climate*, 26(13), 4518-4534.
- 314 Block, K., & Mauritsen, T. (2013). Forcing and feedback in the MPI-ESM-LR coupled model under abruptly  
 315 quadrupled CO<sub>2</sub>. *Journal of Advances in Modeling Earth Systems*, 5(4), 676-691.
- 316 Bony, S., Colman, R., Kattsov, V. M., Allan, R. P., Bretherton, C. S., Dufresne, J.-L., . . . Ingram, W. (2006). How  
 317 well do we understand and evaluate climate change feedback processes? *Journal of Climate*, 19(15), 3445-  
 318 3482.
- 319 Ceppi, P., & Gregory, J. M. (2017). Relationship of tropospheric stability to climate sensitivity and Earth's observed  
 320 radiation budget. *Proceedings of the National Academy of Sciences*. doi:10.1073/pnas.1714308114
- 321 Charney, J. G., Arakawa, A., Baker, D. J., Bolin, B., Dickinson, R. E., Goody, R. M., . . . Wunsch, C. I. (1979).  
 322 *Carbon dioxide and climate: a scientific assessment*: National Academy of Sciences, Washington, DC.

- 323 Cheng, W., Chiang, J. C. H., & Zhang, D. X. (2013). Atlantic Meridional Overturning Circulation (AMOC) in  
324 CMIP5 Models: RCP and Historical Simulations. *Journal of Climate*, 26(18), 7187-7197. doi:10.1175/Jcli-  
325 D-12-00496.1
- 326 Flato, G., Marotzke, J., Abiodun, B., Braconnot, P., Chou, S. C., Collins, W., . . . Rummukainen, M. (2013).  
327 Evaluation of Climate Models. In T. F. Stocker, D. Qin, G.-K. Plattner, M. Tignor, S. K. Allen, J.  
328 Boschung, A. Nauels, Y. Xia, V. Bex, & P. M. Midgley (Eds.), *Climate Change 2013: The Physical  
329 Science Basis. Contribution of Working Group I to the Fifth Assessment Report of the Intergovernmental  
330 Panel on Climate Change* (pp. 741–866). Cambridge, United Kingdom and New York, NY, USA:  
331 Cambridge University Press.
- 332 Friedman, A. R., Hwang, Y.-T., Chiang, J. C., & Frierson, D. M. (2013). Interhemispheric temperature asymmetry  
333 over the twentieth century and in future projections. *Journal of Climate*, 26(15), 5419-5433.
- 334 Geoffroy, O., Saint-Martin, D., Bellon, G., Voldoire, A., Oliv  , D., & Tyt  ca, S. (2013). Transient climate response  
335 in a two-layer energy-balance model. Part II: Representation of the efficacy of deep-ocean heat uptake and  
336 validation for CMIP5 AOGCMs. *Journal of Climate*, 26(6), 1859-1876.
- 337 Gregory, J., Dixon, K., Stouffer, R., Weaver, A., Driesschaert, E., Eby, M., . . . Jungclaus, J. (2005). A model  
338 intercomparison of changes in the Atlantic thermohaline circulation in response to increasing atmospheric  
339 CO<sub>2</sub> concentration. *Geophysical Research Letters*, 32(12).
- 340 Gregory, J., Ingram, W., Palmer, M., Jones, G., Stott, P., Thorpe, R., . . . Williams, K. (2004). A new method for  
341 diagnosing radiative forcing and climate sensitivity. *Geophysical Research Letters*, 31(3).
- 342 Gregory, J. M., Bouffes, N., Griffies, S. M., Haak, H., Hurlin, W. J., Jungclaus, J., . . . Romanou, A. (2016). The  
343 Flux-Anomaly-Forced Model Intercomparison Project (FAFMIP) contribution to CMIP6: investigation of  
344 sea-level and ocean climate change in response to CO<sub>2</sub> forcing. *Geoscientific Model Development*, 9(11),  
345 3993-4017.
- 346 Held, I. M., & Shell, K. M. (2012). Using Relative Humidity as a State Variable in Climate Feedback Analysis.  
347 *Journal of Climate*, 25(8), 2578-2582. doi:10.1175/Jcli-D-11-00721.1
- 348 Held, I. M., Winton, M., Takahashi, K., Delworth, T., Zeng, F., & Vallis, G. K. (2010). Probing the fast and slow  
349 components of global warming by returning abruptly to preindustrial forcing. *Journal of Climate*, 23(9),  
350 2418-2427.
- 351 Heuz  , C., Heywood, K. J., Stevens, D. P., & Ridley, J. K. (2015). Changes in global ocean bottom properties and  
352 volume transports in CMIP5 models under climate change scenarios. *Journal of Climate*, 28(8), 2917-2944.
- 353 Kang, S. M., Frierson, D. M., & Held, I. M. (2009). The tropical response to extratropical thermal forcing in an  
354 idealized GCM: The importance of radiative feedbacks and convective parameterization. *Journal of the  
355 Atmospheric Sciences*, 66(9), 2812-2827.
- 356 Kang, S. M., Held, I. M., Frierson, D. M., & Zhao, M. (2008). The response of the ITCZ to extratropical thermal  
357 forcing: Idealized slab-ocean experiments with a GCM. *Journal of Climate*, 21(14), 3521-3532.
- 358 Lee, S. K., Lumpkin, R., Baringer, M. O., Meinen, C. S., Goes, M., Dong, S., . . . Yeager, S. G. (2019). Global  
359 Meridional Overturning Circulation Inferred From a Data-Constrained Ocean & Sea-Ice Model.  
360 *Geophysical Research Letters*, 46(3), 1521-1530.
- 361 Li, C., von Storch, J.-S., & Marotzke, J. (2013). Deep-ocean heat uptake and equilibrium climate response. *Climate  
362 Dynamics*, 40(5-6), 1071-1086.
- 363 Liu, F., Lu, J., Garuba, O., Leung, L. R., Luo, Y., & Wan, X. (2018a). Sensitivity of Surface Temperature to  
364 Oceanic Forcing via q-Flux Green's Function Experiments. Part I: Linear Response Function. *Journal of  
365 Climate*, 31(9), 3625-3641.
- 366 Liu, F., Lu, J., Garuba, O. A., Huang, Y., Leung, L. R., Harrop, B. E., & Luo, Y. (2018b). Sensitivity of surface  
367 temperature to oceanic forcing via q-flux Green's function experiments Part II: Feedback decomposition  
368 and polar amplification. *Journal of Climate*(2018).
- 369 Manabe, S., & Stouffer, R. J. (1993). Century-scale effects of increased atmospheric CO<sub>2</sub> on the ocean-atmosphere  
370 system. *Nature*, 364(6434), 215.
- 371 Marshall, J., Scott, J. R., Armour, K. C., Campin, J. M., Kelley, M., & Romanou, A. (2015). The ocean's role in the  
372 transient response of climate to abrupt greenhouse gas forcing. *Climate Dynamics*, 44(7-8), 2287-2299.  
373 doi:10.1007/s00382-014-2308-0
- 374 Pendergrass, A. G., Conley, A., & Vitt, F. M. (2018). Surface and top-of-atmosphere radiative feedback kernels for  
375 CESM-CAM5. *Earth System Science Data*, 10(1), 317-324.
- 376 Rose, B. E. J., Armour, K. C., Battisti, D. S., Feldl, N., & Koll, D. D. B. (2014). The dependence of transient climate  
377 sensitivity and radiative feedbacks on the spatial pattern of ocean heat uptake. *Geophysical Research  
378 Letters*, 41(3), 1071-1078. doi:10.1002/2013gl058955

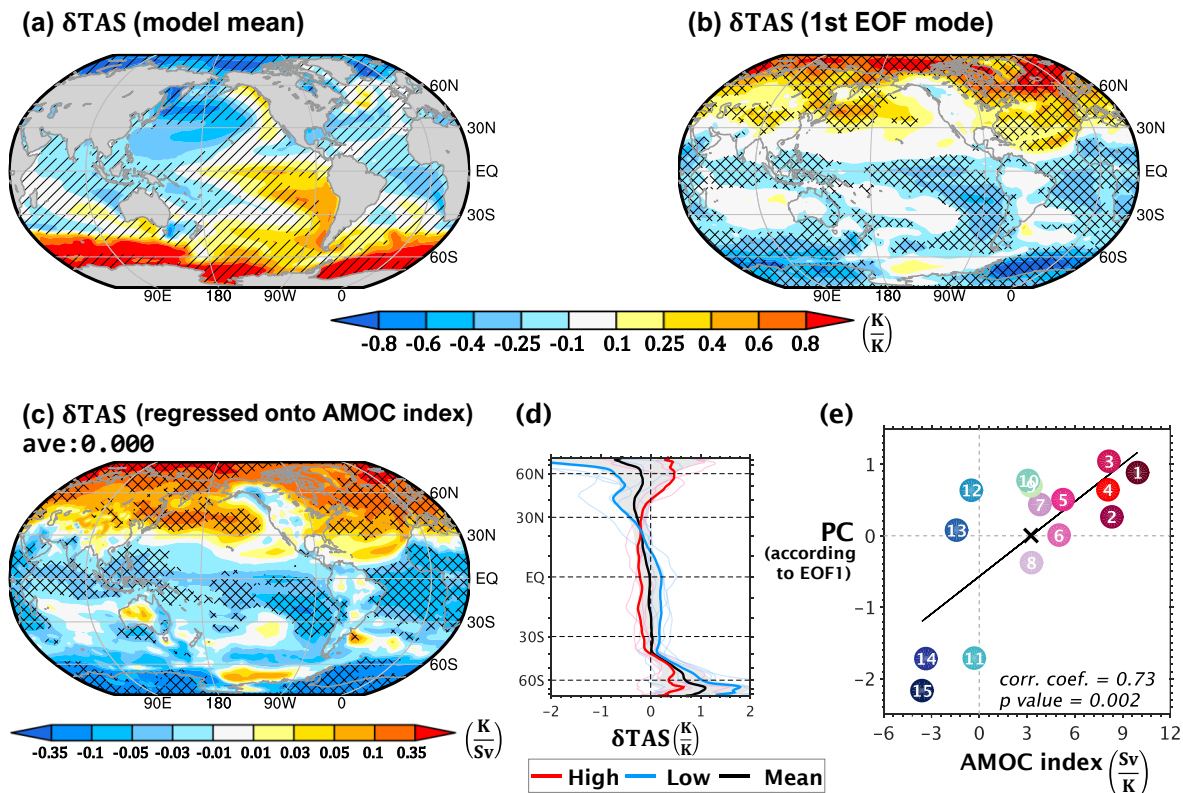
- 379 Rugenstein, M. A. A., Caldeira, K., & Knutti, R. (2016). Dependence of global radiative feedbacks on evolving  
380 patterns of surface heat fluxes. *Geophysical Research Letters*, 43(18), 9877-9885.  
381 doi:10.1002/2016gl070907
- 382 Saenko, O. A., Yang, D., & Myers, P. G. (2017). Response of the North Atlantic dynamic sea level and circulation  
383 to Greenland meltwater and climate change in an eddy-permitting ocean model. *Climate Dynamics*, 49(7),  
384 2895-2910. doi:10.1007/s00382-016-3495-7
- 385 Schmitz Jr, W. J. (1995). On the interbasin-scale thermohaline circulation. *Reviews of Geophysics*, 33(2), 151-173.
- 386 Sgubin, G., Swingedouw, D., Drijfhout, S., Hagemann, S., & Robertson, E. (2015). Multimodel analysis on the  
387 response of the AMOC under an increase of radiative forcing and its symmetrical reversal. *Climate*  
388 *Dynamics*, 45(5-6), 1429-1450.
- 389 Shell, K. M. (2013). Consistent differences in climate feedbacks between atmosphere–ocean GCMs and atmospheric  
390 GCMs with slab–ocean models. *Journal of Climate*, 26(12), 4264-4281.
- 391 Sobel, A. H., Held, I. M., & Bretherton, C. S. (2002). The ENSO signal in tropical tropospheric temperature.  
392 *Journal of Climate*, 15(18), 2702-2706.
- 393 Soden, B. J., Held, I. M., Colman, R., Shell, K. M., Kiehl, J. T., & Shields, C. A. (2008). Quantifying climate  
394 feedbacks using radiative kernels. *Journal of Climate*, 21(14), 3504-3520.
- 395 Stouffer, R., & Manabe, S. (2003). Equilibrium response of thermohaline circulation to large changes in atmospheric  
396 CO<sub>2</sub> concentration. *Climate Dynamics*, 20(7-8), 759-773.
- 397 Stouffer, R. J., Yin, J., Gregory, J., Dixon, K., Spelman, M., Hurlin, W., . . . Hasumi, H. (2006). Investigating the  
398 causes of the response of the thermohaline circulation to past and future climate changes. *Journal of*  
399 *Climate*, 19(8), 1365-1387.
- 400 Swingedouw, D., Mignot, J., Braconnot, P., Mosquet, E., Kageyama, M., & Alkama, R. (2009). Impact of  
401 freshwater release in the North Atlantic under different climate conditions in an OAGCM. *Journal of*  
402 *Climate*, 22(23), 6377-6403.
- 403 Swingedouw, D., Rodehacke, C. B., Olsen, S. M., Menary, M., Gao, Y., Mikolajewicz, U., & Mignot, J. (2015). On  
404 the reduced sensitivity of the Atlantic overturning to Greenland ice sheet melting in projections: a multi-  
405 model assessment. *Climate Dynamics*, 44(11-12), 3261-3279.
- 406 Talley, L. D., Reid, J. L., & Robbins, P. E. (2003). Data-based meridional overturning streamfunctions for the global  
407 ocean. *Journal of Climate*, 16(19), 3213-3226.
- 408 Thompson, D. W., & Wallace, J. M. (2000). Annular modes in the extratropical circulation. Part I: Month-to-month  
409 variability. *Journal of Climate*, 13(5), 1000-1016.
- 410 Trossman, D., Palter, J., Merlis, T., Huang, Y., & Xia, Y. (2016). Large-scale ocean circulation-cloud interactions  
411 reduce the pace of transient climate change. *Geophysical Research Letters*, 43(8), 3935-3943.
- 412 Vial, J., Dufresne, J.-L., & Bony, S. (2013). On the interpretation of inter-model spread in CMIP5 climate sensitivity  
413 estimates. *Climate Dynamics*, 41(11-12), 3339-3362.
- 414 Wang, C. Z., Zhang, L. P., Lee, S. K., Wu, L. X., & Mechoso, C. R. (2014). A global perspective on CMIP5 climate  
415 model biases. *Nature Climate Change*, 4(3), 201-205. doi:10.1038/Nclimate2118
- 416 Webb, M. J., Lock, A. P., Bretherton, C. S., Bony, S., Cole, J. N., Idelkadi, A., . . . Ogura, T. (2015). The impact of  
417 parametrized convection on cloud feedback. *Philosophical Transactions of the Royal Society A:*  
418 *Mathematical, Physical and Engineering Sciences*, 373(2054), 20140414.
- 419 Winton, M., Griffies, S. M., Samuels, B. L., Sarmiento, J. L., & Frölicher, T. L. (2013). Connecting changing ocean  
420 circulation with changing climate. *Journal of Climate*, 26(7), 2268-2278.
- 421 Winton, M., Takahashi, K., & Held, I. M. (2010). Importance of Ocean Heat Uptake Efficacy to Transient Climate  
422 Change. *Journal of Climate*, 23(9), 2333-2344. doi:10.1175/2009jcli3139.1
- 423 Wood, R., & Bretherton, C. S. (2006). On the relationship between stratiform low cloud cover and lower-  
424 tropospheric stability. *Journal of Climate*, 19(24), 6425-6432.
- 425 Zhou, C., Zelinka, M. D., & Klein, S. A. (2016). Impact of decadal cloud variations on the Earth's energy budget.  
426 *Nature Geoscience*, 9(12), 871.
- 427 Zhou, C., Zelinka, M. D., & Klein, S. A. (2017). Analyzing the dependence of global cloud feedback on the spatial  
428 pattern of sea surface temperature change with a Green's function approach. *Journal of Advances in*  
429 *Modeling Earth Systems*, 9(5), 2174-2189.

430

431

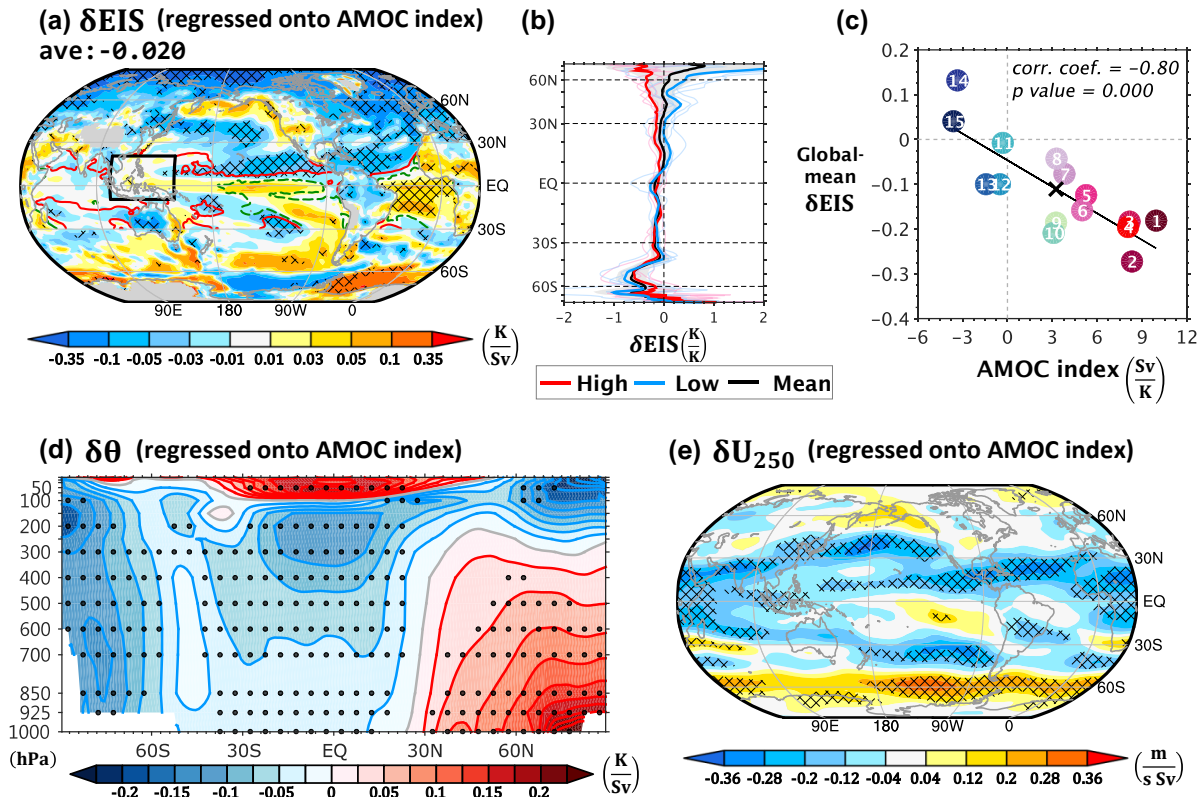


432  
 433 **Figure 1.** (a) The time evolution of AMOC strength in abrupt4 $\times$ CO<sub>2</sub> simulations. The strength at  
 434 year 0 is the 150-year mean in corresponding parallel piControl simulations. The black line  
 435 indicates the multimodel mean, while the thick red (blue) line indicates the high (low) AMOC  
 436 index composite mean, and the thin red (blue/gray) lines are from individual models with high  
 437 (low/medium) AMOC index. (b)  $\delta\lambda$  versus the AMOC index. Each dot is one model, labeled in  
 438 the box and colored according to the AMOC index.  
 439



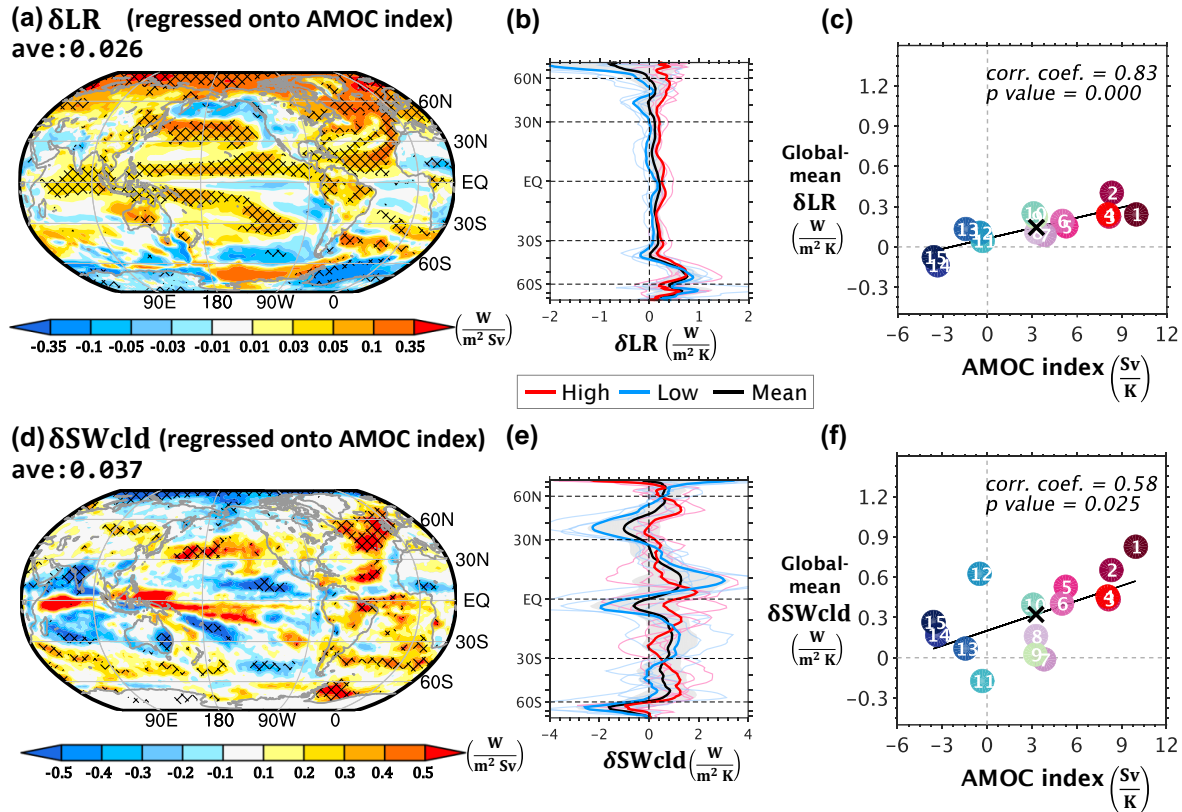
440  
 441 **Figure 2.** (a) Multimodel-mean pattern evolution of surface air temperature ( $\delta$ TAS). Hatching  
 442 denotes an absolute multimodel mean < 1 standard deviation across models. (b) The first EOF  
 443 pattern of  $\delta$ TAS across models. Statistical significance is assessed by regressing  $\delta$ TAS onto the PC  
 444 according to the first EOF. (c) The regression slopes of  $\delta$ TAS against the AMOC index. (d)

445 Zonally-averaged  $\delta$ TAS. The meaning of colored lines is the same as in Figure 1a. The gray  
 446 shading represents the multimodel mean  $\pm 1$  standard deviation (K/K) across models. Meshing in  
 447 (b) and (c) denotes the significance at 95% confidence level. (e) The PC corresponding to the first  
 448 EOF of  $\delta$ TAS versus the AMOC index.  
 449



450  
 451 **Figure 3.** The regression slopes of (a) EIS evolution ( $\delta$ EIS) (d) zonal-mean potential temperature  
 452 evolution ( $\delta\theta$ ), and (e) 250 hPa zonal wind evolution ( $\delta U_{250}$ ) against the AMOC index. Stippling  
 453 and meshing denote the significance at 95% confidence level. Contours in (a) denote the  
 454 anomalous  $\delta$ TAS relative to the warm pool (black box), with solid red (dashed green) indicating a  
 455 more positive (negative)  $\delta$ TAS. This is done only in the tropics. (b) Zonally-averaged  $\delta$ EIS. The  
 456 meaning of colored lines and shading is the same as in Figure 2d. (c) Global-mean  $\delta$ EIS versus the  
 457 AMOC index.





458  
459  
460  
461  
462  
463  
464

**Figure 4.** (a) The regression slopes of lapse-rate feedback evolution ( $\delta LR$ ) against the AMOC index, with meshing denoting the significance at 95% confidence level. (b) Zonally-averaged  $\delta LR$ . The meaning of colored lines and shading is the same as in Figure 2d. (c) The global-mean  $\delta LR$  versus the AMOC index. (d, e, f) Same as (a, b, c) but for shortwave cloud feedback evolution ( $\delta SWcld$ ).